applied optics

Research on scattering models of air particles with variable size distribution and shape distribution

Zhirui Cao[1] and Hanbing Jiang[2,*]

[1]Changchun Institute of Optics, Fine Mechanics and Physics, Chinese Academy of Sciences, Changchun, Jilin 130033, China
[2]Jilin Institute of Chemical Technology, Jilin, Jilin 132022, China
*Corresponding author: caozhirui_0503@163.com

Received 11 January 2019; revised 18 March 2019; accepted 19 March 2019; posted 25 March 2019 (Doc. ID 357273); published 25 April 2019

This paper proposes a new method for solving an average scattering model of air particles with variable size distribution and shape distribution, analyzes the effects of size distribution and shape distribution of particles on the new scattering model, and compares the difference of scattering models simulated by different shapes. The results indicate that the accuracy of the new model is much better than that of the Mie model and the previous average scattering model, and the maximum relative errors of the new model for calculating the intensity distribution and polarization are 12% and 13%, respectively. The maximum relative deviation between Mueller matrix phase functions is less than 7% when the effective radius and variance of air particles are the same, the maximum relative deviation between Mueller matrix phase functions reaches more than 700% when the shape distribution of air particles changes, and the maximum relative deviation between Mueller matrix phase functions is less than 18% when the shapes used to simulate the scattering model are changed.

https://doi.org/10.1364/AO.58.003370

1. INTRODUCTION

In some high-precision optical testing and calibration work, the error caused by scattering by airborne particles cannot be ignored. For example, the Chinese Academy of Sciences is developing a large space telescope with an external dimension of 8.5 mm × 2.7 mm × 3.8 mm and a point source transmittance (PST) design value of less than 4.6×10^{-9}, and scientists had planned to create a clean environment of ISO class 3 in a 600 mm × 600 mm laboratory to achieve the test accuracy of PST [1–3]. Similar requirements for a clean room have emerged in the calibration of large polarization spectral cameras [4–7]. Compared to the establishment of large clean rooms with high standards, quantitative analysis and correction of the errors caused by scattering by airborne particles is more economical and feasible. Therefore, we need to establish a high-precision air scattering model to accurately simulate the scattering intensity distribution and scattering polarization distribution of airborne particles.

There are existing methods that could be used to accurately solve the scattering model of a spherical or nonspherical single particle. Several methods are known, such as Mie theory [8,9], the Rayleigh method [10,11], the T matrix method [12,13], finite difference time domain (FDTD) [14,15], multiresolution time domain (MRTD) [16,17], method of moments (MoMs) [18], discrete dipole approximation (DDA) [19], the geometric optics approximation (GOA) method [20], the extended boundary condition method (EBCM) [21], the separation of variables method (SVM) [22], and so on. When air particles have variable size distribution and shape distribution, it is not practical to accurately solve the scattering model of the particles by listing the scattering properties of each particle. To simplify the operation, the existing methods have simplified the size distribution and shape distribution of air particles. The most common simplification method is to simplify the shape distribution of particles to a single spherical or nonspherical shape; for this reason, some scholars have also focused on what shape should be used to simulate the scattering model more accurately [23]. However, these simplified methods are essentially not different from Mie theory, and the accuracy of the scattering models can be greatly improved. We proposed an air average scattering model, which can simulate the intensity distribution of scattered light more accurately, but cannot accurately simulate the polarization distribution of scattered light [24,25].

In this paper, a new average scattering model is proposed to obtain more accurate polarization simulations of scattered light. In addition, the effects of the size distribution and shape distribution of air particles on the new scattering model are quantitatively analyzed, and the differences of scattering models

simulated by different shapes are compared to verify the adaptability of the new model.

2. MODELING OF AIR SCATTERING

Air scattering primarily consists in the scattering of gas molecules and suspended particles; the scattering model of gas molecules can be solved by the Rayleigh method [26]. Thus, this paper mainly researches the scattering model of suspended particles with an equivalent spherical diameter greater than 0.1 μm. The existing methods are used to solve the scattering model of a single particle with a certain size and shape, and random particles with a certain size distribution and shape distribution are used to simulate the average scattering model.

The scattering model of particles is described by the Mueller matrix, and the relationship between the Stokes matrix and the Mueller matrix has the following expression [27]:

$$\begin{bmatrix} I \\ Q \\ U \\ V \end{bmatrix} = \begin{bmatrix} F_{11}(\theta) & F_{12}(\theta) & 0 & 0 \\ F_{12}(\theta) & F_{22}(\theta) & 0 & 0 \\ 0 & 0 & F_{33}(\theta) & F_{34}(\theta) \\ 0 & 0 & -F_{34}(\theta) & F_{44}(\theta) \end{bmatrix} \times \begin{bmatrix} I_0 \\ Q_0 \\ U_0 \\ V_0 \end{bmatrix}. \tag{1}$$

In Eq. (1), θ is the scattering angle, I and I_0 are the intensity of scattered light and incident light, respectively; Q and Q_0 are the intensity difference of the two components when the electric vector is decomposed into x-axis and y-axis components; U and U_0 are the intensity difference of the two components when the electric vector is decomposed into +45-degree and −45-degree components; V and V_0 are the intensity difference of the two components when the electric vector is decomposed into the right-circular polarization component and the left-circular polarization component.

The Mueller matrix elements, after having been averaged by using the size distribution and shape distribution of particles, will have the following expression:

$$\overline{F_{XX}} = \frac{\sum_{k=1}^{m} W_k \int_r F_{XX}(\varepsilon_k, r) K_{\text{sca}}(\varepsilon_k, r) S_P(\varepsilon_k, r) f(r) \mathrm{d}r}{\sum_{k=1}^{m} W_k \int_r K_{\text{sca}}(\varepsilon_k, r) S_P(\varepsilon_k, r) f(r) \mathrm{d}r}. \tag{2}$$

In Eq. (2), all terms indexed with k refer to a group of particles with a certain shape. $\overline{F_{xx}}$ represents the element of the Mueller matrix after having averaged the air particles by size distribution and shape distribution; $F_{xx}(\varepsilon_k, r)$ is an element of the Mueller matrix corresponding to the particles with a certain shape, $K_{\text{sca}}(\varepsilon_k, r)$ is the scattering coefficient; $S_P(\varepsilon_k, r)$ indicates the geometric projection area of particles along the light transmission direction; ε_k represents the shape parameter; $f(x)$ is the size distribution function of particles; and W_k is the weight coefficient of particles with a certain shape representing the shape distribution of the particles.

The weight coefficients are solved by a least squares method through the intensity and polarization data of incident light and scattered light, as shown in Eq. (3):

$$\mathrm{MIN}(S) = \Sigma_\theta \left\{ \begin{array}{l} \left(\frac{I - \overline{F_{11}(\theta)} I_0 - \overline{F_{12}(\theta)} Q_0}{I} \right)^2 + \left(\frac{Q - \overline{F_{12}(\theta)} I_0 - \overline{F_{22}(\theta)} Q_0}{I} \right)^2 + \\ \left(\frac{U - \overline{F_{33}(\theta)} U_0 - \overline{F_{34}(\theta)} V_0}{I} \right)^2 + \left(\frac{V - \overline{F_{34}(\theta)} U_0 - \overline{F_{44}(\theta)} Q_0}{I} \right)^2 \end{array} \right\}. \tag{3}$$

In Eq. (3), MIN(S) represents the minimum value for the right-hand side of the equation.

3. CALCULATION AND VALIDATION RESULTS

A. Statistics of Size Distribution and Shape Distributions of Air Particles

We measured the size distributions of particles under ISO Class 8, ISO Class 7, and ISO Class 6 by using an air particle counter. The air particle counter is composed of an air pump, a laser scattering cavity, a convergent lens, a photodetector, and a signal processing system. The air pump draws the air into the laser scattering cavity at a certain sampling rate, and the scattered light is collected on the photodetector through the convergent lens. The signal processing system calculates the number of particles per unit volume of air based on the count of electrical pulses and determines the sizes of the particles based on the intensity of the electrical pulse signal. The results are shown in Fig. 1, where the y axis indicates that the particle concentration is equal to or greater than the size considered.

The results indicated that the size distribution function $f(r)$ roughly satisfied the index distribution indicated by

$$\frac{\int_{r_1}^{\infty} f(r)\mathrm{d}r}{\int_{r_2}^{\infty} f(r)\mathrm{d}r} = \left(\frac{r_1}{r_2} \right)^{-n}. \tag{4}$$

The index n varied slightly with the air cleanliness. The lower the air cleanliness level, the larger the index, that is, the smaller the proportion of large particles. The fitting value of the index and the fitting error of the size distribution function under different air cleanliness are shown in Fig. 2.

We observed the deposition of air particles on test strips under different air cleanliness conditions by a 50-fold microscope and roughly judged the shape characteristics of air particles, as shown in Fig. 3. The observation results showed that the larger particles in the air were mainly rope-shaped, which

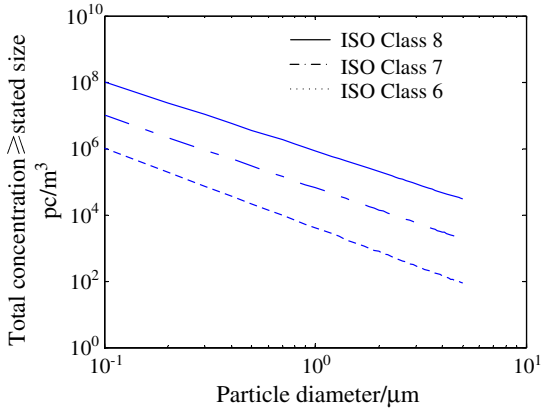

Fig. 1. Measured data of the particles' size distribution.

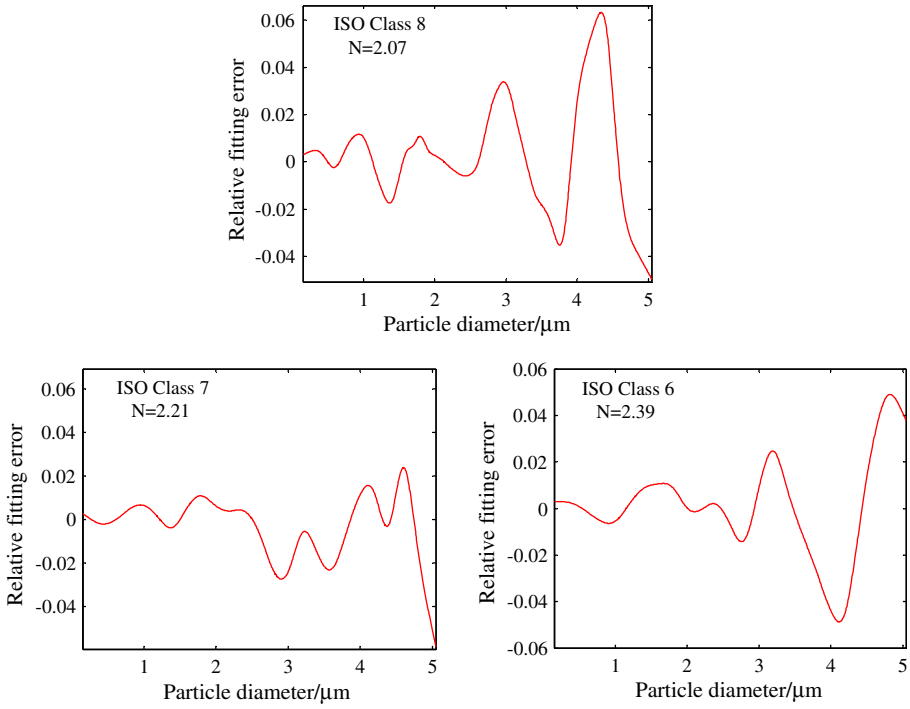

Fig. 2. Fitting value of the index and the fitting error of the size distribution function.

may be the clothing fiber debris caused by the activities of laboratory personnel; we simulated the shapes of these particles by cylindrical shapes with 10 different diameter-to-length ratios. The smaller particles were approximately ellipsoidal, which may be aerosols composed of dust, sulfuric acid, nitric acid, and so on; therefore, we simulated the shapes of particles by ellipsoidal shapes with 10 different aspect ratios.

The aspect ratio of ellipsoidal particles was expressed by a/b, and the diameter-to-length ratio of cylindrical particles was expressed by D/L, as shown in Fig. 4. The 10 ellipsoidal aspect ratios used to simulate the shape distribution of air particles were uniformly distributed in the range of [0.3,3.0], and the 10 cylindrical aspect ratios were uniformly distributed in the range of [0.05,1.0].

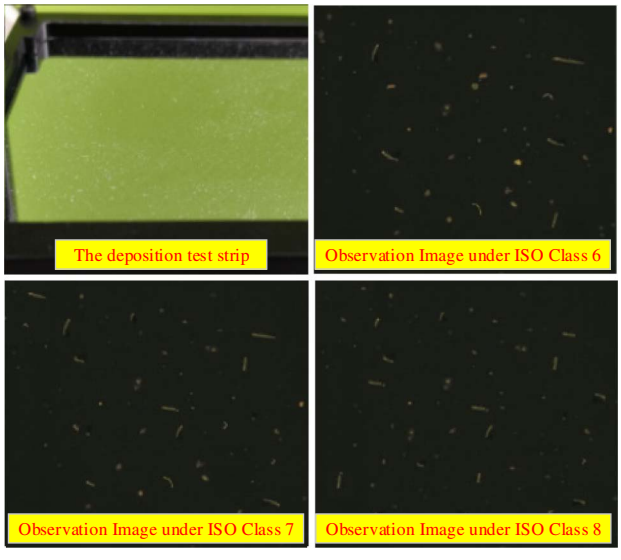

Fig. 3. Sediments of air particles observed using the microscope.

B. Solution and Verification of the New Model

To solve the undetermined weight coefficients W_k in Eq. (5), we built a test system, as shown in Fig. 5. The test system was located in a dark room with an air cleanliness below IS0 class 8, and it included a pulse laser, an optical collimated system with a diameter of 100 mm, a photodetector with lens hood, and a polarizer. The laser light was not polarization, such that the Stokes matrix was the matrix (1,0,0, 0) T. The polarization state of scattered light was measured by a polarizer and a photodetector. The lens hood was used to suppress the off-axis light of the photodetector. In addition, the usage of the light trap was crucial to prevent the light from being scattered back by the inner wall of the laboratory to the measurement region, thus improving the measurement precision.

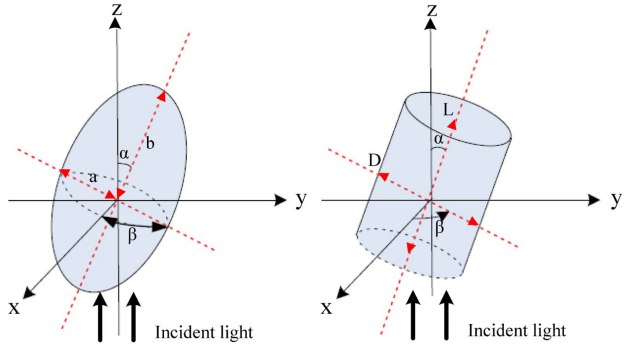

Fig. 4. Illustration of parameters of ellipsoidal and cylindrical particles.

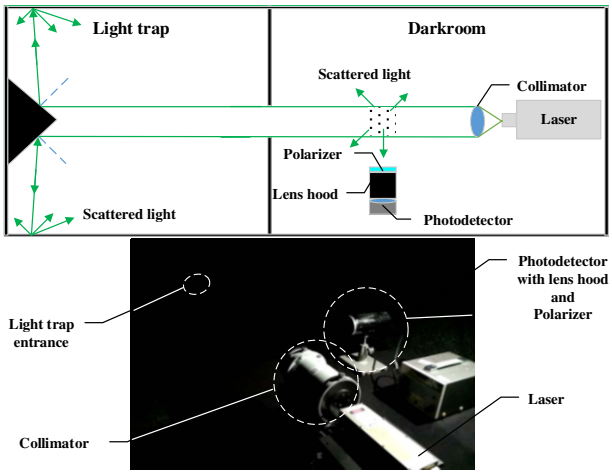

Fig. 5. Model for optical path verification.

The Stokes matrix elements of the scattered light were measured at scattering angles of 30°, 60°, 90°, 120°, and 150°, and the average distance from the measurement point to the scattering particles was $r = 1$ m. Based on these measurements, the average Mueller matrix elements were calculated and compared to those calculated by the Mie model and the previous average scattering model, as shown in Fig. 6.

As can be seen in Fig. 6, the Mueller matrix elements calculated by the previous average scattering model and the new model were greatly different from those calculated by the Mie model. The Mueller matrix elements $\overline{F_{11}}$ calculated by the previous average scattering model and the new model were close to each other, and the same was true for $\overline{F_{12}}/\overline{F_{11}}$. However, the other Mueller matrix elements calculated by the previous average scattering model and the new model were quite different from each other.

We analyzed the reason why $\overline{F_{11}}$ and $\overline{F_{12}}/\overline{F_{11}}$ calculated by the previous average scattering model and the new model were

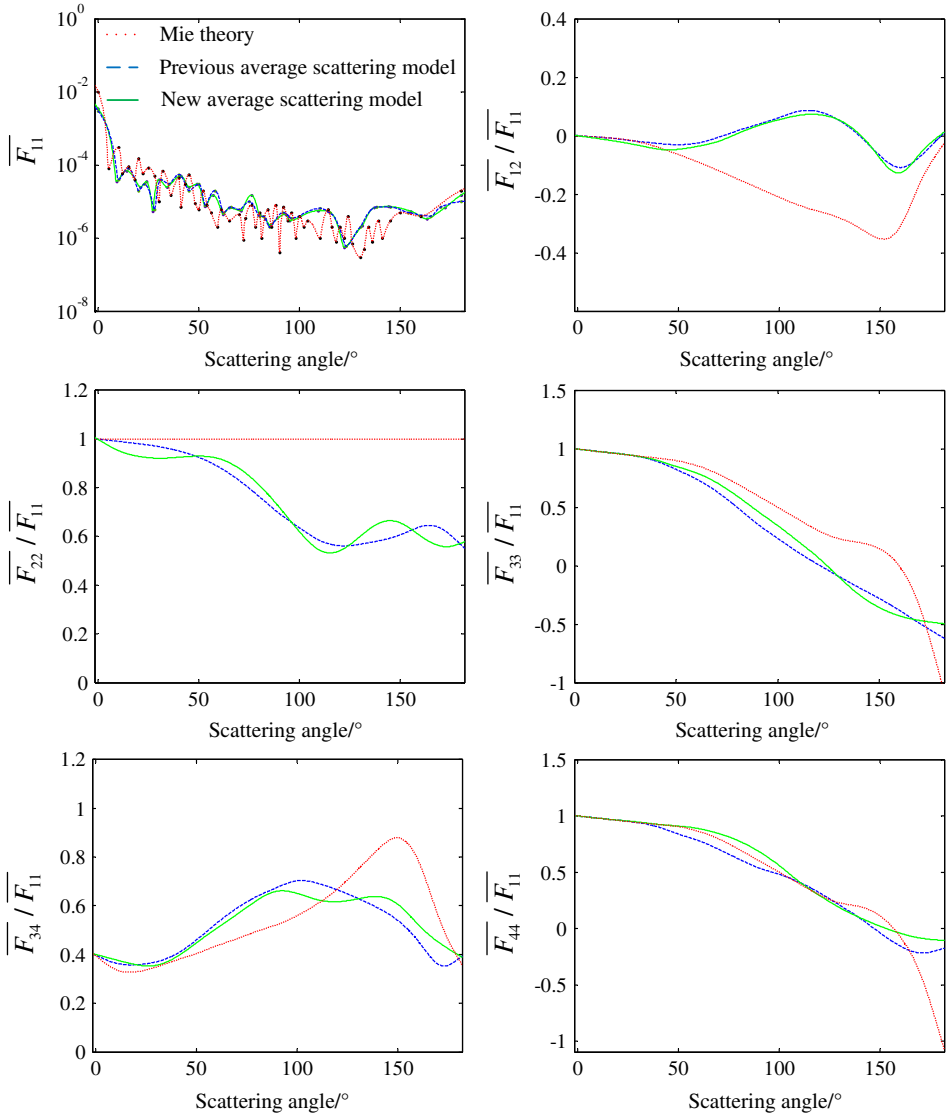

Fig. 6. Average Mueller matrix element and the Mueller matrix element of the equivalent spherical particles calculated by using the Mie scattering theory.

close to each other, while the other Muller matrix elements are quite different. In the previous average scattering model, we used only the intensity of incident light and scattered light to simulate the weight coefficient of particles. So, the calculation results of $\overline{F_{11}}$ and $\overline{F_{12}}/\overline{F_{11}}$ are accurate, but the calculation results of other Mueller matrix elements may be quite different from the actual situation. In the new model, we use the intensity and polarization distribution of incident light and scattered light to simulate the weight coefficients of particles; this can improve the calculation accuracy of the other Muller matrix elements. The results shown in Fig. 6 indicated that the calculation results of Muller matrix elements were different when the polarization distributions were taken into account, which also reflected the necessity of using both intensity and polarization distributions to calculate the weight coefficients of particles.

To validate the accuracy of different models, we calculated the intensities and degree of polarizations (DOPs, as shown in Eq. (5) [28]) of the scattered light by the Mie model, the previous average scattering model, and the new model. The results are reported in Figs. 7 and 8, together with the measurement results. The DOP calculation is as follows:

$$\mathrm{DOP} = \frac{\sqrt{Q^2 + U^2 + V^2}}{I}. \tag{5}$$

As can be observed from Fig. 7, the maximum relative deviation between the intensities calculated by the previous average scattering model and the measured data was less than 10%; the maximum relative deviation between the intensities calculated by the new model and the measured data was less than 12%; and the maximum relative deviation between the intensities calculated by the Mie model and the measured data exceeded 480%. When calculating the intensities of the scattered light, the accuracy of the new model was much better than that of the Mie model but slightly worse than that of the previous average scattering model. This was mainly due to the additional consideration of the polarization distribution characteristics in solving the new model. As can be observed from Fig. 8, the maximum relative deviation between the DOP calculated by the new model and the measured data was less than 13%;

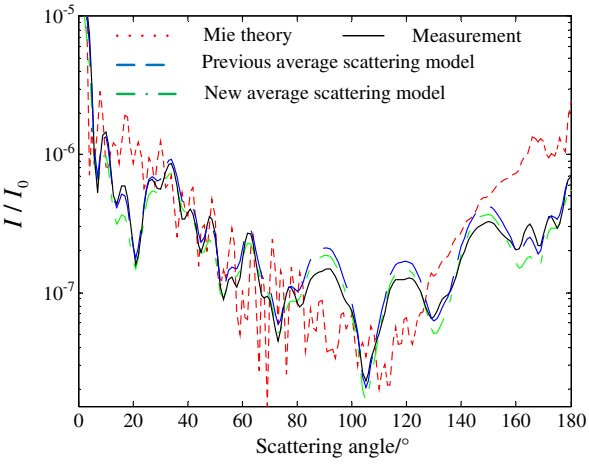

Fig. 7. Comparison between the scattering light intensities calculated by different models and the measured data.

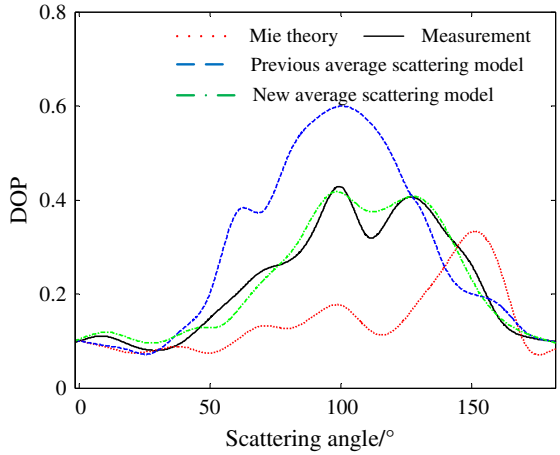

Fig. 8. Comparison between the DOP calculated by different models and the measured data.

the maximum relative deviation between the DOP calculated by the previous average scattering model and the measured data was less than 49%; and the maximum relative deviation between the DOP calculated by the Mie model and the measured data exceeded 220%. When calculating the DOP of the scattered light, the new model had the best precision. On the whole, the new model was more comprehensive and accurate.

4. QUANTITATIVE ANALYSIS OF THE NEW MODEL

A. Effect of Particle Size Distribution on Scattering Model

We fixed the shape distribution of particles, and the size distribution of particles was changed to study the effect of the size distribution of particles on the scattering model. We calculated the average Mueller matrix phase function $\overline{F_{11}}$ when the size distributions of particles were gamma distributions and log-normal distributions, respectively, and used the relative deviations $\eta(\theta)$ between the calculation results of the two distributions. The calculation results and the relative deviations are shown in Fig. 9.

As can be observed from Fig. 9, as long as the effective radius and effective variance were the same for different size distributions, the average Mueller matrix phase functions were basically consistent, and the maximum relative deviation was less than 7%. When the effective radius was small, the Mueller matrix phase function presented a more uniform scattering function and had a relatively smooth function curve. When the effective radius gradually increased, the Mueller matrix phase function exhibited a tendency of forward and backward scattering enhancement, and the function curve oscillated greatly with the scattering angle.

B. Effect of Particle Shape Distribution on Scattering Model

The size distribution of particles was fixed, and the shape distribution of particles was changed to study the effect of the shape distribution of particles on the scattering model. Ten ellipsoids with different aspect ratios and 10 cylindrical shapes

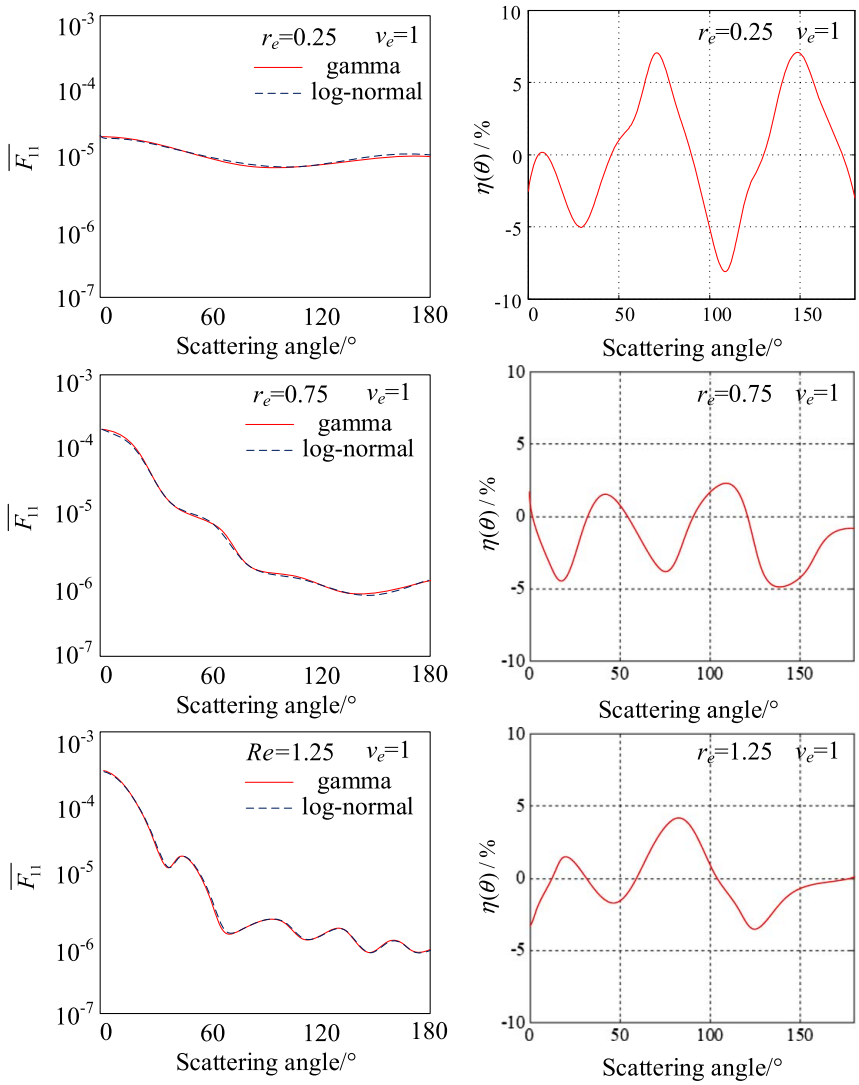

Fig. 9. Calculation results of average Mueller matrix phase function and relative deviations.

with different diameter-to-length ratios were used to simulate the shape distribution of particles; the ellipsoidal aspect ratios were uniformly distributed in the range of [0.3,3.0], and the cylindrical aspect ratios were uniformly distributed in the range of [0.05,1.0]. In case 1, the sum of the weight coefficients representing ellipsoidal particles is equal to 0.5, and the sum of the weight coefficients representing cylindrical particles is equal to 0.5. In case 2, the sum of the weight coefficients representing ellipsoidal particles is equal to 0.8, and the sum of the weight coefficients representing cylindrical particles is equal to 0.2. In case 3, the sum of the weight coefficients representing ellipsoidal particles is equal to 0.2, and the sum of the weight coefficients representing cylindrical particles is equal to 0.8. We calculated the average Mueller matrix phase function $\overline{F_{11}}$ with the new model in different cases, and got the relative deviations $\eta(\theta)$ between the results. The calculation results and the relative deviations are shown in Fig. 10.

As can be observed from Fig. 10, when the shape distributions of particles changed, the Mueller matrix phase function calculated by the new model changed significantly, and the maximum relative deviation reached 700%. It means that the new model can sensitively reflect the change of scattering characteristics caused by the shape distribution of particles. In contrast, the Mie model does not have this capability. It can only reflect the change of scattering characteristics caused by the equivalent volume of particles. So, this is one of the main advantages of the new model compared to the Mie model.

C. Difference of Scattering Models Simulated by Different Shapes

The size distribution and the shape distribution of particles were held fixed, and the shapes chosen for simulating the scattering model were changed to study the difference of scattering models simulated by different shapes. In case 1, 10 ellipsoidal shapes and 10 cylindrical shapes were used to simulate the scattering model; the ellipsoidal aspect ratios were uniformly distributed in the range of [0.3,3.0], and the cylindrical aspect ratios were uniformly distributed in the range of [0.05,1.0]. In case 2, five ellipsoidal shapes and 15 cylindrical shapes were used to simulate the scattering model; the ellipsoidal aspect

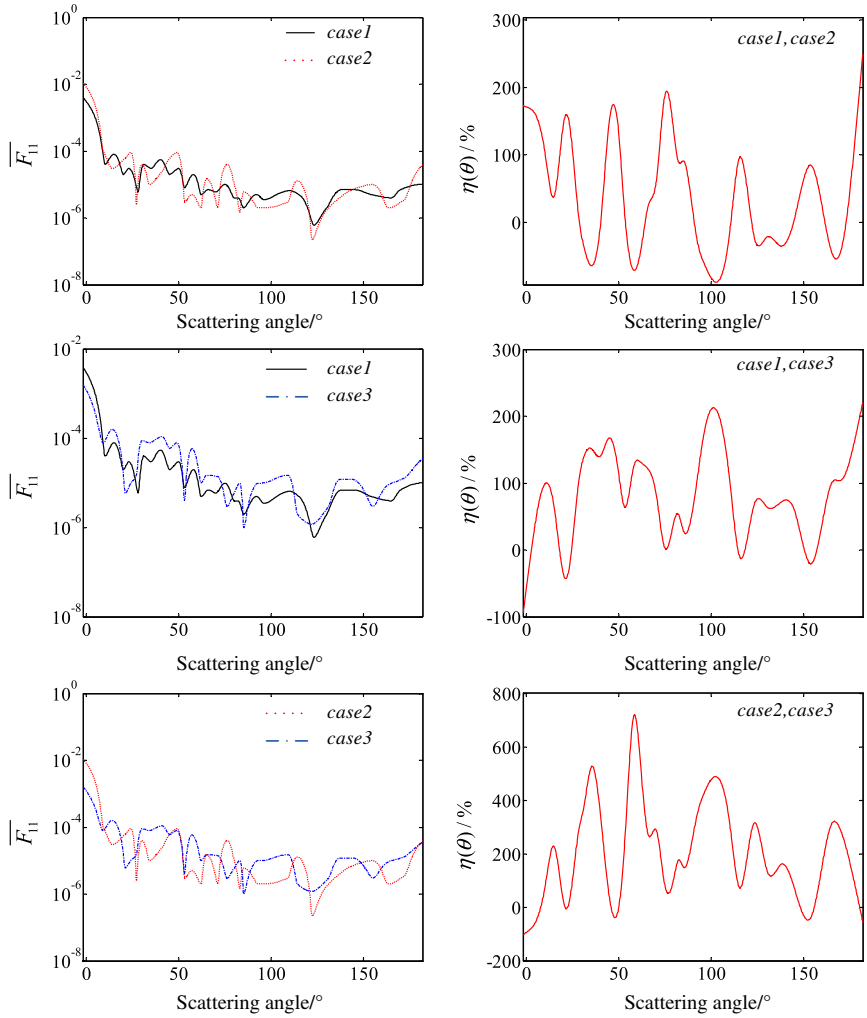

Fig. 10. Calculation results of average Mueller matrix phase function and relative deviations.

ratios were uniformly distributed in the range of [0.3,3.0], and the cylindrical aspect ratios were uniformly distributed in the range of [0.05,1.0]. In case 3, 15 ellipsoidal shapes and five cylindrical shapes were used to simulate the scattering model; the ellipsoidal aspect ratios were uniformly distributed in the range of [0.3,3.0], and the cylindrical aspect ratios were uniformly distributed in the range of [0.05,1.0]. We calculated the average Mueller matrix phase function $\overline{F_{11}}$ with the new model in different cases, and got the relative deviations $\eta(\theta)$ between the calculation results. The calculation results and the relative deviations are shown in Fig. 11.

As can be observed from Fig. 11, when the shapes chosen to simulate the scattering model were changed, the calculation results of the average Mueller matrix phase function changed slightly, and the maximum relative deviation was less than 18%.

5. CONCLUSIONS

In this paper, we proposed a new method of solving an average scattering model of air particles with variable size distribution and shape distribution. The maximum relative errors of the intensity distribution and polarization calculated by the new model were 12% and 13%, respectively, and the accuracy of the new model was better than that of Mie model and the previous average scattering model.

Based on the new model, we analyzed the effects of size distribution and shape distribution of air particles on the scattering model and compared the difference of scattering models simulated by different shapes. The results showed that when the effective radius and variance of air particles were the same, the scattering models were basically the same, and the maximum relative deviation between the average Mueller matrix phase functions was less than 7%. When the shape distribution of air particles changed, the scattering models changed greatly, and the maximum relative deviation between the scattering phase functions reached more than 700%. When the shapes used to simulate the scattering model changed, the normalized weighting coefficients of these shapes changed correspondingly, but the scattering model was basically the same; the maximum relative deviation of the average Mueller matrix phase functions was less than 18%.

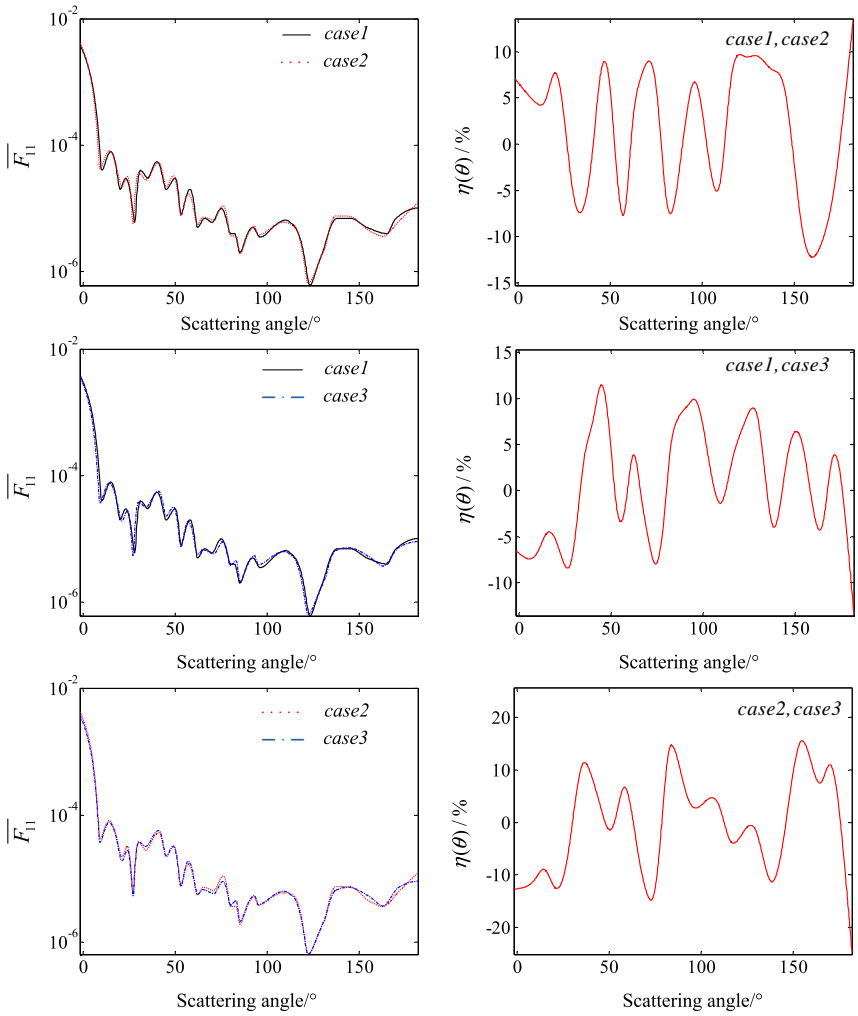

Fig. 11. Difference of the average Mueller matrix phase function simulated by different shapes.

REFERENCES

1. Q. Chen, Z. Ma, X. Li, Z. Pang, L. Xu, and Z. Li, "Stray light measurement for point source transmittance of space optical systems," Proc. SPIE **9684**, 96842V (2016).
2. F. Grochocki and J. Fleming, "Stray light testing of the OLI telescope," Proc. SPIE **7794**, 77940W (2010).
3. T. Whitman, "Testing a critical stray light path of the James Webb space telescope," Proc. SPIE **7731**, 77310L1 (2010).
4. G. van Harten, D. J. Diner, B. J. Daugherty, B. E. Rheingans, M. A. Bull, F. C. Seidel, R. A. Chipman, B. Cairns, A. P. Wasilewski, and K. D. Knobelspiesse, "Calibration and validation of airborne multiangle spectropolarimetric imager (AirMSPI) polarization measurements," Appl. Opt. **57**, 4499–4513 (2018).
5. A. Virkki, J. Markkanen, J. Tyynelä, J. I. Peltoniemi, and K. Muinonen, "Polarized backscattering by clusters of spherical particles," Opt. Lett. **40**, 3663–3666 (2015).
6. A. Roy, R. Kumar Singh, and M. M. Brundavanam, "Sensing polarization rotation through scattering media," in *Frontiers in Optics* (The Optical Society, 2018), p. FM4C.6.
7. A. J. Brown, T. I. Michaels, S. Byrne, W. Sun, T. N. Titus, A. Colaprete, M. J. Wolff, and G. Videen, "The science case for a modern, multi-wavelength, polarization-sensitive LIDAR in orbit around mars," J. Quantum Spectrosc. Radiat. Transfer **153**, 131–143 (2015).
8. M. L. Marasinghe, M. Premaratne, and D. M. Paganin, "Generation of coherence vortex networks from systems of several Mie-scattering particles," Proc. SPIE **8458**, 845832 (2012).
9. K. J. Zhou and J. Chen, "A simple analysis of extinction spectra of cancerous and normal prostate tissues in near infrared range using a size discrete particle distribution and Mie scattering model," Proc. SPIE **9315**, 93150T (2015).
10. J. E. Harvey and R. N. Pfisterer, "Comparison of the GHS Smooth and the Rayleigh-Rice surface scatter theories," Proc. SPIE **9961**, 996103 (2016).
11. D. Zhang, S. Hao, L. Wang, and Q. Zhao, "Depolarization of laser beam propagating through atmosphere based on multiple Rayleigh scattering model," Proc. SPIE **10021**, 100211Y (2016).
12. U. Tricoli and K. Pfeilsticker, "Scattering of electromagnetic radiation based on numerical calculation of the T-matrix through its integral representation," Proc. SPIE **9232**, 923208 (2014).
13. L. Bi and P. Yang, "Modeling of light scattering by biconcave and deformed red blood cells with the invariant imbedding T-matrix method," Proc. SPIE **18**, 055001 (2013).
14. X. Lin, N. Wan, L. Weng, H. Zhu, and J. Du, "FDTD method and models in optical education," Proc. SPIE **10452**, 104524J (2017).
15. C. Leiner, S. Schweitzer, and V. Schmidt, "Multi-scale simulation of an optical device using a novel approach for combining ray-tracing and FDTD," Proc. SPIE **8781**, 87810Z (2013).
16. S. Hu, T. Gao, and L. Hao, "Simultaneously simulating the scattering properties of nonspherical aerosol particles with different sizes by the MRTD scattering model," Opt. Express **25**, 17872–17891 (2017).
17. L. Gong, Z. Wu, M. Gao, and T. Qu, "Analysis of composite/difference field scattering properties between a slightly rough optical surface and multi-body defects," Appl. Opt. **57**, 2165–2171 (2018).

18. M. Yu, Y. Han, Z. Cui, and H. Sun, "Scattering of a Laguerre-Gaussian beam by complicated shaped biological cells," J. Opt. Soc. Am. **35**, 1504–1510 (2018).
19. Y. Wang, L. Ran, J. Dai, Z. Liu, Z. Xiong, T. Zhang, H. Chen, and H. Ma, "Differentiation of suspended particles by polarized light scattering at 120°," Opt. Express **26**, 22419–22431 (2018).
20. P. Yang, K. N. Liou, L. Bi, C. Liu, B. Yi, and B. A. Baum, "On the radiative properties of ice clouds: light scattering, remote sensing, and radiation parameterization," Adv. Atmos. Sci. **32**, 32–63 (2015).
21. L. Bi and P. Yang, "Tunneling effects in electromagnetic wave scattering by nonspherical particles: A comparison of the Debye series and physical-geometric optics approximations," J. Quantum Spectrosc. Radiat. Transfer **178**, 93–107 (2016).
22. M. Xie, Q. Zhang, S. Chen, and F. Zha, "A lithological classification method from fully polarimetric SAR data using Cloude-Pottier decomposition and SVM," Proc. SPIE **9674**, 967405 (2015).
23. O. Dubovik, A. Sinyuk, T. Lapyonok, B. N. Holben, M. Mishchenko, P. Yang, T. F. Eck, H. Volten, O. Munoz, B. Veihelmann, and W. J. Van der Zande, "Application of spheroid models to account for aerosol particle nonsphericity in remote sensing of desert dust," J. Geophys. Res. **111**, D11208 (2006).
24. Z. Cao, X. Xun, and Y. Fu, "Analysis of the impact of air scattering on point source transmittance," Appl. Opt. **57**, 6664–6670 (2018).
25. A. J. Brown, "Equivalence relations and symmetries for laboratory, LIDAR, and planetary Müeller matrix scattering geometries," J. Opt. Soc. Am. A **31**, 2789–2794 (2014).
26. A. J. Brown and Y. Xie, "Symmetry relations revealed in Mueller matrix hemispherical maps," J. Quantum Spectrosc. Radiat. Transfer **113**, 644–651 (2012).
27. R. Kalibjian, "Stokes polarization vector and Mueller matrix for a corner-cube reflector," Opt. Commun. **240**, 39–68 (2004).
28. X. Zhao and T. D. Visser, "Degree of polarization in the focal region of a lens," J. Opt. Soc. Am. **35**, 1518–1522 (2018).